TASK QUARTERLY 9 No 1, 115–132

UNSTEADY SHOCK WAVE – TURBULENT BOUNDARY LAYER INTERACTION IN THE LAVAL NOZZLE

PIOTR DOERFFER[1], OSKAR SZULC[1]
AND FRANCO MAGAGNATO[2]

[1] *Institute of Fluid-Flow Machinery,*
Polish Academy of Sciences,
Fiszera 14, 80-952 Gdansk, Poland,
{doerffer, osmark}@imp.gda.pl

[2] *Institute für Strömungslehre, Universität Karlsruhe,*
Kaiserstr. 12, D-76128 Karlsruhe, Germany
magagnato@mach.uni-karlsruhe.de

(Received 2 September 2004)

Abstract: The flow in transonic diffusers and supersonic air intakes often becomes unsteady due to shock wave-boundary layer interaction. Oscillations may be induced by natural separation unsteadiness or forced by boundary conditions. Significant improvements of CFD tools, increased computer resources and the development of experimental methods have again drawn the attention of researchers to this topic.

Forced oscillations of a transonic turbulent flow in an asymmetric two-dimensional Laval nozzle have been considered to investigate the problem. A viscous, perfect gas flow was numerically simulated using SPARC, a Reynolds-averaged compressible Navier-Stokes solver, employing a two-equation, eddy viscosity, turbulence closure in the URANS approach.

For time-dependent and stationary flow simulations, Mach numbers upstream of the shock between 1.2 and 1.4 were considered. Comparison of computed and experimental data for steady states generally gave acceptable agreement. In the case of forced oscillations, a harmonic pressure variation was prescribed at the exit plane resulting in shock wave motion. Excitation frequencies between 0Hz and 1024Hz were investigated at a constant pressure amplitude.

The main result of the work is the relation between the amplitude of shock wave motion and the excitation frequency in the investigated range. Increasing excitation frequency resulted in decreasing amplitude of the shock movement. At high frequencies, a natural mode of shock oscillation (of small amplitude) was observed, which was insensitive to forced excitement.

Keywords: unsteady transonic flow, shock wave, nozzle flow

Nomenclature

X – the streamwise coordinate
Y – the crosswise coordinate
y^+ – non-dimensional distance from the wall

t – time
f – frequency
k – turbulent kinetic energy
τ – turbulent time scale
ε – the dissipation rate of turbulent kinetic energy
Tu – turbulence level at the inlet
μ – dynamic viscosity
μ_t – eddy viscosity at the inlet
γ – the ratio of specific heats, C_P/C_V
R – the gas constant
q – the wall heat flux
ρ – density
u, v – velocity components
E – total energy
Re – the Reynolds number
Ma – the Mach number
$p(t)$ – pressure varying in time
A_p – amplitude of pressure varying in time
P – pressure level
P_0 – total pressure at the inlet
T_0 – total temperature at the inlet
C_L – the lift coefficient
C_d – the drag coefficient
CFL – the Courant-Friedrichs-Levy number

1. Introduction

Recently unsteady transonic flows, mostly of two-dimensional geometries but also in three-dimensional ones, have again received considerable attention and an extensive description of inviscid and viscous flows can be found in literature. This is due to the significantly improved experimental and numerical tools available nowadays. In comparison to the one-dimensional approach, the present research can reflect all details of the shock wave-boundary layer interaction structure.

Our investigations were carried out in a convergent-divergent nozzle. The case was examined with Mach numbers upstream of the shock ranging from 1.2 to 1.4. An ideal gas flow was considered with a Reynolds number of approximately $\mathrm{Re} = 1.4 \cdot 10^6$ based on the flow parameters in the throat [1].

Because unsteady and separated transonic flows were involved, numerical methods capable of solving time-dependent, mass-weighted, Reynolds-averaged, compressible Navier-Stokes equations were considered. The SPARC finite volume computer code [2] was used to calculate the results with the help of parallel computing (MPI) on a Beowulf type cluster of PCs.

The experimental investigation concerned only stationary flow with steady conditions at the nozzle outlet. Measurements included static pressures and a schlieren visualisation of the flow structure. Only numerical results are available for the unsteady cases. Steady state measurements and computations were carried out solely to verify our numerical methods.

The main goal of the unsteady computations was to explore the influence of frequency (ranging from 0Hz to 1024Hz) on the shock wave motion (for constant

amplitude pressure changes at the outlet). It was achieved with the help of a new turbulence model [3, 4], utilizing a non-linear, cubic, Craft-Launder-Suga [5] formulation. Spectral interaction between the driving unsteady phenomena and turbulence was negligible due to low values of frequency.

Two new observations were made. A maximum of the amplitude was observed at very low frequencies, where the moving shock wave passed beyond the stationary shock boundaries. This happened only when the shock movement was very slow, *viz.* below 50 Hz. At approximately 500 Hz, the shock wave response disappeared. For higher excitations, a new natural oscillation appeared, with a much lower frequency, which was insensitive to forced back pressure fluctuations. It was a shorter time step that enabled us to capture the appearance of natural shock oscillations. The observed shock movement was connected with the formation and shedding of vortices from the separation zone downstream of the shock. Additionally, static pressure fluctuations were analyzed at a few significant locations in the stream-wise direction.

2. Previous work

The majority of earlier work was done using simplified inviscid and laminar gas dynamics theories. Just to mention a few, Adamson (1972, [6]) and later Adamson and Richey (1973, [7]) used the general gas dynamics potential equation and the Bernoulli equation with the small-disturbance theory and a similarity transformation to analyze and compute numerically solutions of unsteady transonic flows with and without planar shock waves in two-dimensional symmetric channels for stationary and varying-in-time wall shapes. After abandoning the similarity solutions, the proposed methodology was extended to arbitrary wall shapes and initial conditions with oscillating back pressure (Richey and Adamson, 1976, [8]), curved shocks in asymmetric channels (Chan and Adamson, 1978, [9]), and large-amplitude motion (Adamson, Messiter and Liou, 1978, [10]). Later, a comparison was presented of the shock wave motion due to the fluctuating back pressure and the boundaries' movement (Messiter and Adamson, 1984, [11]).

With the help of the small disturbance theory Rizetta and Chin (1979, [12]) investigated the effect of frequency on transonic flow over the NACA 64A010 airfoil for three different types of motion. Bölcs, Fransson and Platzer (1989, [13]) utilized full Euler equations to study numerically the large-amplitude motion of shock waves in a quasi one-dimensional nozzle and in a two-dimensional channel with a sinusoidal bump. Their investigations were later extended to an experimental and numerical comparison of the shock motion for a fixed geometry of the nozzle, employing various measuring techniques and a solution of the Euler equations (Ott, 1992, [14], and Ott, Bölcs and Fransson, 1995, [15]).

Continuously increasing accessible computer power enabled the use of mass-weighted Reynolds-averaged Navier-Stokes equations with proper turbulence models. Extensive experimental and numerical investigations of natural and forced oscillations of shock waves were carried out. A two-dimensional and fully turbulent, unsteady and separated transonic flow over a thick circular arc foil was studied and computed with help of an algebraic turbulence model by Seegmiller, Marvin and Levy (1978, [16]) and compared with experimental data. Chen, Sajben and Kroutil (1979, [17]) measured

the natural oscillations of a shock wave in separated diffuser flow, while Liou and Coakley (1984, [18]) compared measured self-excited and forced fluctuations of weak and strong shock waves with numerical computations based on thin-layer Navier-Stokes equations with the low-Reynolds k-ω^2 two-equation turbulence model. Shock buffeting over bicircular airfoil was computed and compared with experiment by Arnone, Liou and Povinelli (1995, [19]), on the basis of Navier-Stokes equations with an algebraic Baldwin and Lomax turbulence model. Gerolymos, Vallet, Bölcs and Ott (1996, [20]) investigated the influence of three-dimensional effects on the transonic flow in a nozzle by means of a k-ε turbulence closure. More recently, Bron, Ferrand and Fransson (2002, [21]) explored non-linear interactions in a two-dimensional nozzle configuration using the Wilcox k-ω turbulence model. Very interesting results of the Reynolds number's influence on the unsteady flow through a critical nozzle have been presented by Setoguchi, Matsuo and Kim [22].

All previous work concerning forced shock wave oscillations in nozzles underline the fact that the amplitude of the shock movement depends on both the amplitude and frequency of imposed back pressure changes. Moreover, the shock movement amplitude decreases with increasing excitation frequency. An average unsteady shock position for oscillating back pressure does not agree with the steady state position. An unsteady flow field can be very different from a steady flow field.

3. The experimental arrangement and test conditions

The normal shock wave was located in the divergent part of the nozzle defined by the adequate pressure level at the outlet. The upper wall of the divergent part was convex, unlike the bottom wall, which was flat (see Figure 1). The Mach numbers upstream of the shock were between 1.2 and 1.4, depending on the shock's position.

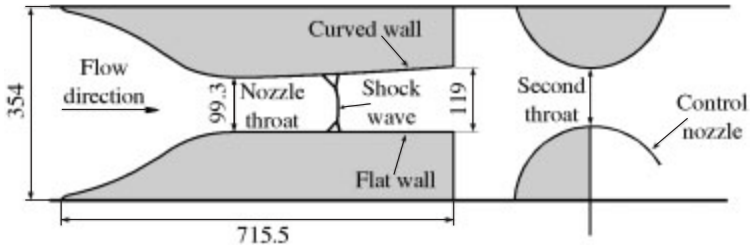

Figure 1. The test section

Glass windows at the divergent section of the nozzle allowed for the use of the schlieren visualization method. Fifty seven pressure taps were uniformly spaced at 5 mm intervals within the area of the shock wave motion. For ten positions of the shock wave schlieren images were taken and static pressure distributions were measured. Total pressure and temperature at the inlet were related to ambient conditions. Pressure at the outlet was set by the control nozzles to achieve the desired shock wave position.

4. The numerical method of solution

The present investigation was carried out with a cell-centered block-structured SPARC code parallelized with a Message Passing Interface (MPI). This code solves numerically compressible, mass-weighted, Reynolds-averaged Navier-Stokes equations in generalized coordinates with several turbulence models. The algorithm uses a semi-discrete approach, utilizing a finite-volume, density-based formulation for spatial discretization and either an explicit Runge-Kutta type or an implicit LU-SSOR [23] method for integration in time.

In order to accelerate convergence, the local time stepping and the implicit residual averaging techniques are included in the explicit approach. Additionally, the full multigrid (FMG) strategy with V-cycles is used. To damp numerical oscillations, the artificial dissipation models is used, both the original blending of the 2^{nd} and 4^{th}-order Jameson-Smith-Turkel switch and a SLIP scheme as proposed by Tatsumi *et al.* [24, 25]. This leads to good convergence rates and shock wave resolution. In our study a very efficient implicit dual-time-stepping scheme was chosen for the time-accurate simulations, which allowed us to utilize all acceleration techniques developed for explicit algorithms.

From the various turbulence closures implemented in the code, the two-equation, low-Reynolds turbulence model of Craft-Launder-Suga was chosen in both the linear and the non-linear adaptive k-τ formulation. The $\tau = k\varepsilon$ turbulent time scale was chosen instead of the dissipation rate of turbulent kinetic energy, ε, to simplify the implementation of the boundary condition in the code ($k = \tau = 0$ at the walls). The linear model was sufficient for time-independent solutions, while a new adaptive turbulence approach was used for the unsteady calculations, based on a non-linear stress-strain relation, which adapts itself automatically to the spatial and temporal resolution of the computational domain.

Second-order, central-difference spatial discretization and the third-order, three-stage Runge-Kutta method (CFL = 2.2) with a SLIP scheme and four-grid multigrid proved to be sufficient for steady state predictions. For a test case with fluctuating back-pressure, we utilized a switch scheme together with a second order, implicit, dual-time-stepping formulation with the same Runge-Kutta method.

The four-block, body-fitted, structured computational grid was prepared with the help of algebraic methods of orthogonal mesh generation and additional elliptical smoothing (Figure 2). In order to find a grid-independent solution, three meshes with different numbers of computational cells were considered.

The steady state computations were performed on coarse (4800), intermediate (20 000) and fine (78 000) grids. The difference between solutions obtained for the intermediate and the fine mesh was negligible. The intermediate mesh proved to be adequate for unsteady cases and more economical as far as computational resources were concerned.

The considered grids were very smooth and regular in the region of the shock wave motion. Computational meshes were reconstructed after the initial tests in accordance with the boundary layer development in the channel. For the grid-independent solution, it was necessary for the non-dimensional distance of the first point adjacent to the wall to be of the order of $y^+ = 1$ (so that it would lie deep in the

viscous sub-layer of the boundary layer). This value was of the order of unity for the whole boundary layer, which was true for the fine as well as the intermediate mesh. the inlet and outlet planes were situated more upstream and downstream compared to the experimental test section in order to assure mesh orthogonality and improved numerical accuracy in this region. Moreover, it prevented flow recirculation at the outlet plane and led to better convergence of the numerical solution. The considered grids were very smooth and regular in the region of shock wave motion.

Total pressure, total temperature and an imposed flow direction with isentropic relations were used to obtain all information at the inlet. Measurements of the characteristic length scale of turbulence and turbulence level at the inlet boundary were not available. A turbulence level of $\mathrm{Tu} = 3\%$ and a physically consistent value of the ratio of eddy viscosity to dynamic viscosity of $\mu_t/\mu = 10$ were assumed on the basis of previous investigations. We set the total temperature at $T_0 = 307\,\mathrm{K}$ and the total pressure at $P_0 = 100\,432\,\mathrm{Pa}$ for all the unsteady cases. Values measured at the inlet were utilized for the steady state calculations.

Values of constant outlet static pressure for the steady cases were chosen to obtain the same shock wave positions as in the experiment. Harmonic oscillations were prescribed for the unsteady cases according to the following function: $p(t) = \bar{p} + A_p/2\sin(2\pi f t)$, where $\bar{p}$ is the average unsteady pressure, A_p – a constant amplitude, f – frequency, and t – time. The amplitude of pressure changes was taken to be $A_p = 5\,\mathrm{kPa}$, with an unsteady average exit pressure of $\bar{p} = 70\,273\,\mathrm{Pa}$. This method of imposing a time-dependent boundary condition for the Runge-Kutta method time advancement reduced the formal accuracy of the space-time method to the first order locally and the second order globally, independently of the spatial operator [26].

The computed frequencies and the respective time steps are summarized in Table 1. There were from 16 to a maximum of 125 time steps (in the dual-time-stepping approach) per one period of oscillations.

The walls were defined with the no-slip of velocity and adiabatic ($q = 0$) conditions; $k = \tau = 0$ was set at the wall for the turbulent quantities.

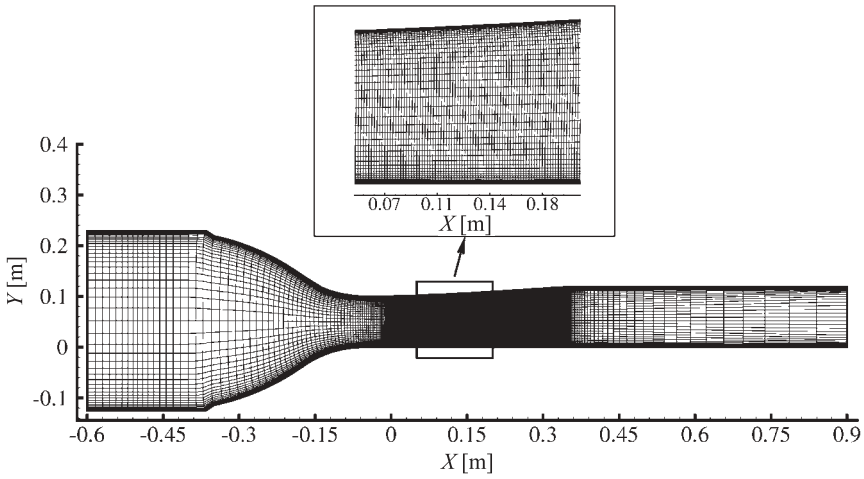

Figure 2. The nozzle geometry and the intermediate mesh

Table 1. The unsteady flow parameters

Frequency f [Hz]	Time step Δt [s]	Amplitude A_p [kPa]	Number of time steps per period
0.5	$2.0 \cdot 10^{-2}$	5	100
8	$1.0 \cdot 10^{-3}$	5	125
64	$2.5 \cdot 10^{-4}$	5	63
128	$5.0 \cdot 10^{-4}$	5	16
256	$2.5 \cdot 10^{-4}$	5	16
512	$1.25 \cdot 10^{-4}$	5	16
1024	$6.25 \cdot 10^{-5}$	5	16

The upstream-extended channel length assured the development of boundary layer (and k and τ profiles minimizing the influence of the inlet boundary condition. The outlet plane, far downstream from the region of interest, minimized the non-physical constant pressure assumption.

Computations in SPARC are usually started from a simple, homogeneous distribution with constant flow parameters throughout the flow-field. For the time dependent cases, the flow was initialized together with fluctuating pressure at the outlet on all the considered grids. The fluid was modeled as a viscous perfect gas. The specific heat ratio was $\gamma = 1.4$, while the gas constant was equal to $R = 287\text{m}^2\text{s}^{-2}\text{K}$. The dynamic viscosity was dependent on the temperature only, according to Sutherland's law. Turbulent and laminar heat exchange conditions were based on the assumption of constant Prandtl numbers, laminar $\text{Pr} = 0.72$ and turbulent $\text{Pr}_t = 0.9$.

The performed tests proved a reduction of the residuals by four orders of magnitude to be sufficient convergence criteria for steady and unsteady cases (on all meshes in the multigrid approach and for all transport equations considered, see Figures 3 and 4).

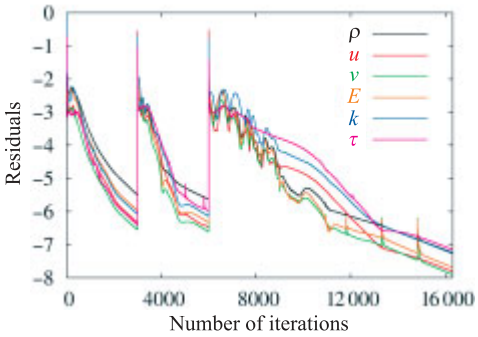

Figure 3. Convergence history for steady-state computation on the coarse, intermediate and fine meshes, $\text{Ma} = 1.3$

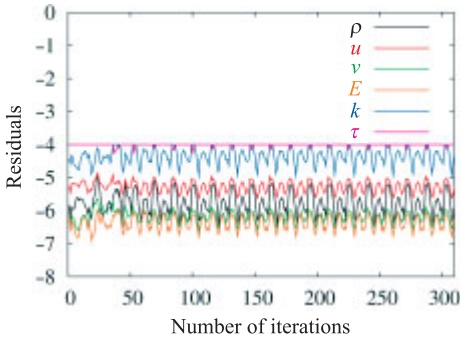

Figure 4. Convergence history for unsteady computation on the intermediate mesh, $f = 256\text{Hz}$

The convergence judgment was also based on global parameters such as lift, C_L, and drag, C_d, coefficients (treated only as integral parameters, insignificant in this case). Obtaining a constant value of C_d for the steady flow and the periodic variation of C_d for the unsteady cases is shown in Figures 5 and 6.

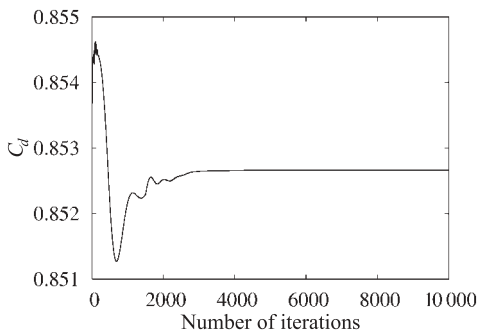

Figure 5. Time history of the drag coefficient, C_d, for steady-state computation, Ma = 1.3

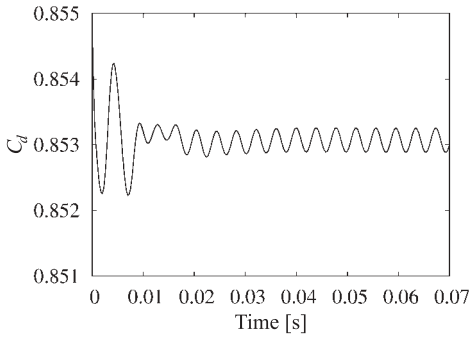

Figure 6. Time history of the drag coefficient, C_d, for unsteady computation, $f = 256$ Hz

The imposition of fluctuating back pressure on the coarser meshes in the full multigrid approach shortened the transient phase and thus minimized the computational effort. Data continued to be collected for analysis for at least one period after the transient phase. For the higher frequencies the time taken by the flow to stabilize was comparable to the period of fluctuations. It was found that more inner steps (in fictitious time) were needed when fewer physical time steps per one period of oscillations were used. For quasi-steady (very low) frequencies, the transient phase practically disappeared.

5. A comparison of experimental and numerical data for steady flow

Figure 7 presents the measured and computed static pressure distributions at the bottom wall of the nozzle for all ten positions of the shock wave (within the range of 0.15 m). The chosen locations are in the region of numerically simulated shock motion. A qualitative and quantitative comparison gives acceptable coincidence, although small discrepancies can be observed. These are due to the inability of the 2D numerics to capture the effect of boundary layer development, which includes the side walls in the real channel. It was assumed that the shock wave position should be the same for the calculations and the experiment. This caused different values of static pressure at the outlet in relation to the wind tunnel measurements. Moreover, the artificial dissipation model, SLIP, lacked weak boundary layer separation at the upper wall of the nozzle, which was present in the experiment. The visible differences in the pressure minima upstream of the shock are directly linked to the difference in the maximum Mach number at about $\Delta \mathrm{Ma} = 0.03$.

The static pressure distribution in the middle of the channel presented in Figure 8 corresponds to Figure 7. It is worth mentioning that a region of local acceleration (expansion) of the flow exists just downstream of the shock wave, which is marked by a circle in Figure 8. This effect is due to the thickening of the boundary layers downstream of the region of shock-boundary layer interaction.

Figures 9, 10 and 11 present an example of flow with a Mach number of Ma = 1.34 upstream of the shock. A contour plot of the Mach number is shown in Figure 9. The experimental schlieren image in Figure 10 is compared with its

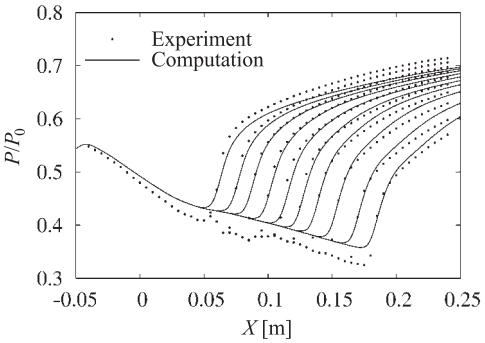

Figure 7. Static pressure distribution at the wall of the nozzle

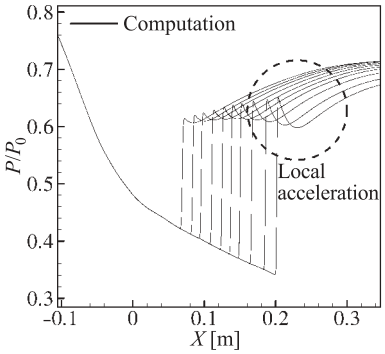

Figure 8. Static pressure distribution in the middle of the nozzle

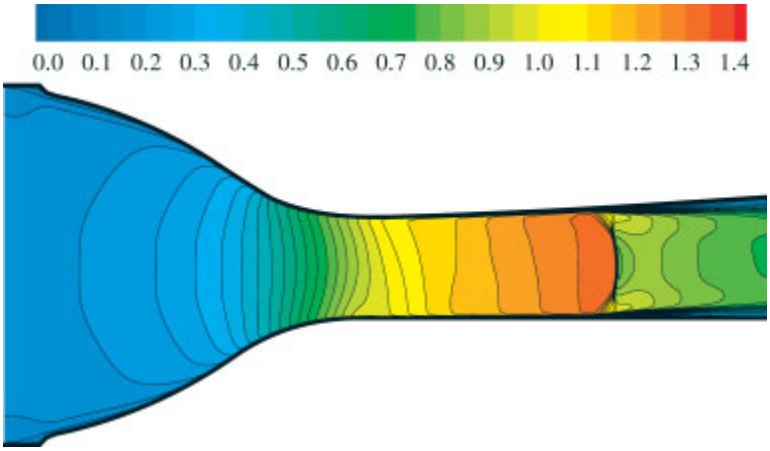

Figure 9. Isolines of Mach number, Ma = 1.34

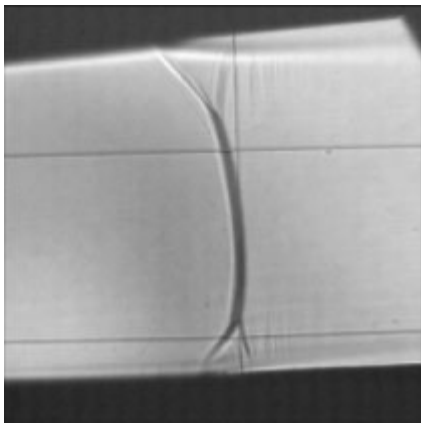

Figure 10. Experimental schlieren picture, Ma = 1.34

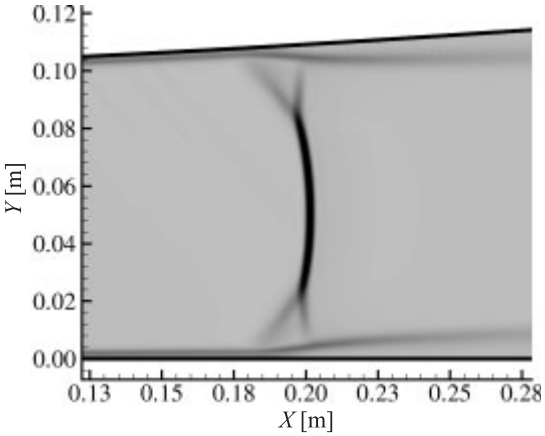

Figure 11. Numerical schlieren picture, Ma = 1.34

numerical simulation in Figure 11. The coincidence of the obtained results is very good and positively verifies the numerical methods used.

6. Results of the unsteady calculations

The oscillations of back pressure at the outlet of the nozzle caused shock wave movement in the range of 0.1 m, with shock upstream maximum Mach numbers ranging from Ma = 1.18 to Ma = 1.35. Figure 12 presents the static pressure distribution in the middle of the channel for three steady-state cases with pressures at the outlet given as $p(t) = \bar{p} + A_p/2$, $p(t) = \bar{p}$ and $p(t) = \bar{p} - A_p/2$.

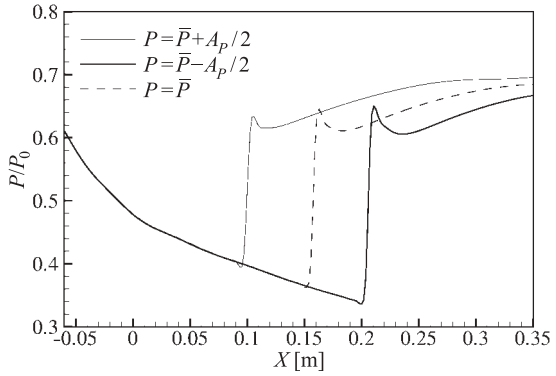

Figure 12. Static pressure distributions in the middle of the nozzle for average and limiting shock positions

The time-dependent shock wave position, based on the pressure minimum in the middle of the channel and at the wall, for at least one period of oscillations, is presented in Figure 13 for the frequencies of 0.5, 8, 64, 128, and 256 Hz. Apparently, the shock wave oscillates harmonically with the frequency of imposed pressure fluctuation, with an amplitude decreasing with increasing frequency. The mean position of the shock wave does not correspond to the steady state solution with $P_{\text{ext}} = \bar{p}$ and depends on the frequency as well.

The relative difference in shock wave position between the middle of the channel and the wall, due to the shock-boundary layer interaction, is changing during one period of oscillations, although no phase lag between these two motions is observed. The amplitude of the shock motion at the wall is smaller than in the middle of the channel and this trend decreases with increasing frequency. The λ-foot for Ma = 1.35 is much greater than for Ma = 1.18: the higher the Mach number, the larger the distance between the main shock and the beginning of interaction at the wall. For low frequencies, the shock motion sweeps the whole range of shock location and the increase of the λ-foot plays a significant role. At high frequencies of excitation the forced shock movement is small; hence the size of the λ-foot does not change much.

The most important conclusion is that for intermediate frequencies (from 50 Hz to 512 Hz) the amplitude of the shock wave motion is inversely proportional to the imposed frequency (Figure 14), which is in accordance with the literature. A local maximum of amplitude has been found in the region of very low frequencies

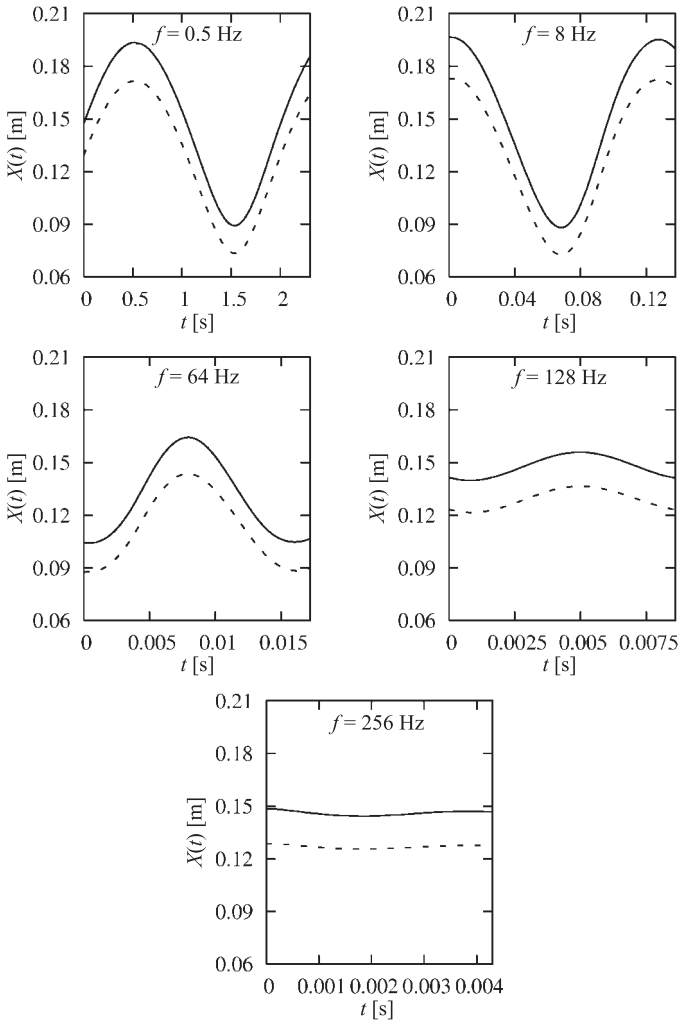

Figure 13. Instantaneous shock wave position in the middle of the channel (solid line) and at the wall (dashed line)

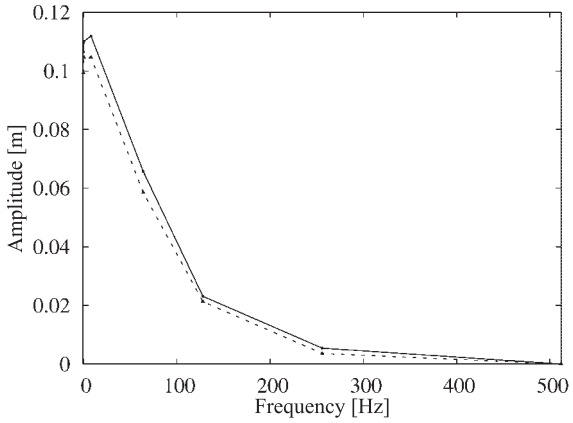

Figure 14. Relation between imposed frequency and amplitude of the shock wave motion in the middle of the channel (solid line) and at the wall (dashed line)

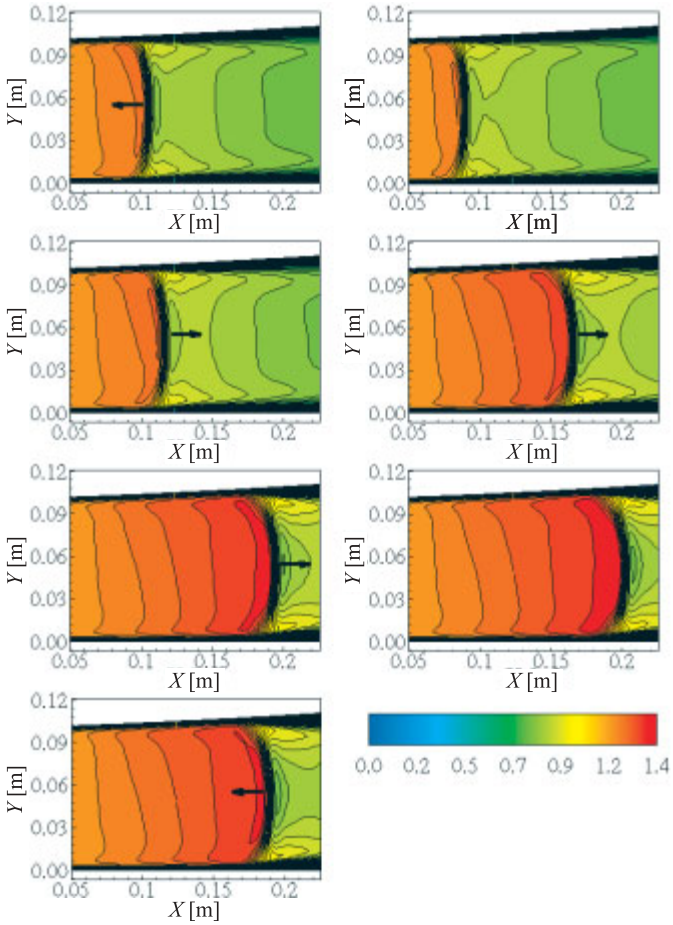

Figure 15. Isolines of the Mach number, $f = 8\,\mathrm{Hz}$

($f < 50\,\mathrm{Hz}$). Such behavior was previously found during measurements with a similar configuration and flow parameters by only one of the authors (Liou *et al.* [18]). The confirmation of these results suggests the necessity of further investigation into this phenomenon.

Our results have also shown that for calculations with frequencies greater than 512Hz the position of the shock wave are unaffected by the pressure changes at the outlet (within the accuracy of mesh resolution). Nevertheless, natural oscillation of low frequency occurs.

The case with shock wave motion of the largest amplitude and the frequency of 8Hz is presented in Figure 15 for illustration. Time-dependent isolines of the Mach number in the region of shock wave movement are shown together with the corresponding static pressure distribution in the middle of the channel (Figure 16). The Mach number varies from $\mathrm{Ma} = 1.18$ (the most upstream shock) to $\mathrm{Ma} = 1.35$ (the most downstream shock). The arrows in Figure 15 indicate the direction of shock movement.

Instantaneous static pressure signals for four representative points in the middle and at the wall of the nozzle are presented in Figure 17. The first point remains in

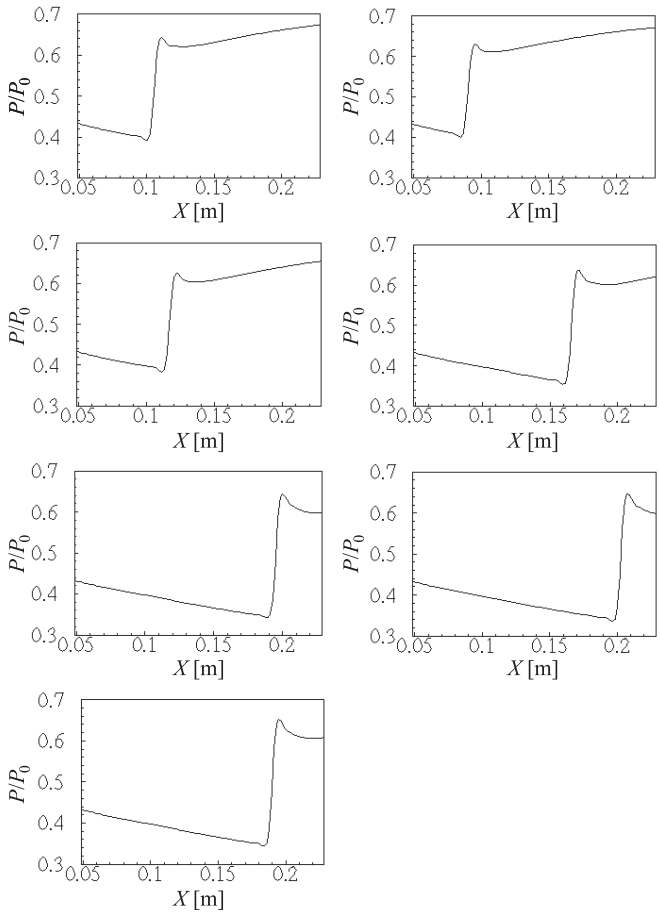

Figure 16. Pressure distribution in the middle of the nozzle, $f = 8\,\mathrm{Hz}$

the supersonic region ($X = 0$), where the pressure signal is constant at all times due to the disturbances' inability to propagate upstream of the shock wave.

The second characteristic point corresponds to the x position of the shock wave taken from the steady state computation with exit pressure $P_{\mathrm{ext}} = \bar{p}$; $X = 0.15\,\mathrm{m}$ for the middle of the channel and $X = 0.13\,\mathrm{m}$ for the wall. The shock wave always passes this point during a period of oscillation and produces a strongly non-harmonic signal. It is especially clearly visible for the middle of the channel, where a sudden pressure jump is connected with the shock's passage. The effect is much weaker at the wall.

The next point is at $X = 0.3\,\mathrm{m}$, which remains in the subsonic region downstream of the shock. The shock wave never reaches or passes this point. At this point, pressure is only subject to mild, periodic changes of amplitude decreasing with increasing frequency.

The last monitored point is at $X = 0.9\,\mathrm{m}$, which corresponds to the outlet of the nozzle. The amplitude and frequency of pressure changes at this plane are strictly connected with the boundary condition imposed. Stagnation pressure downstream the oscillating shock wave changes in accordance with the strength of the shock wave.

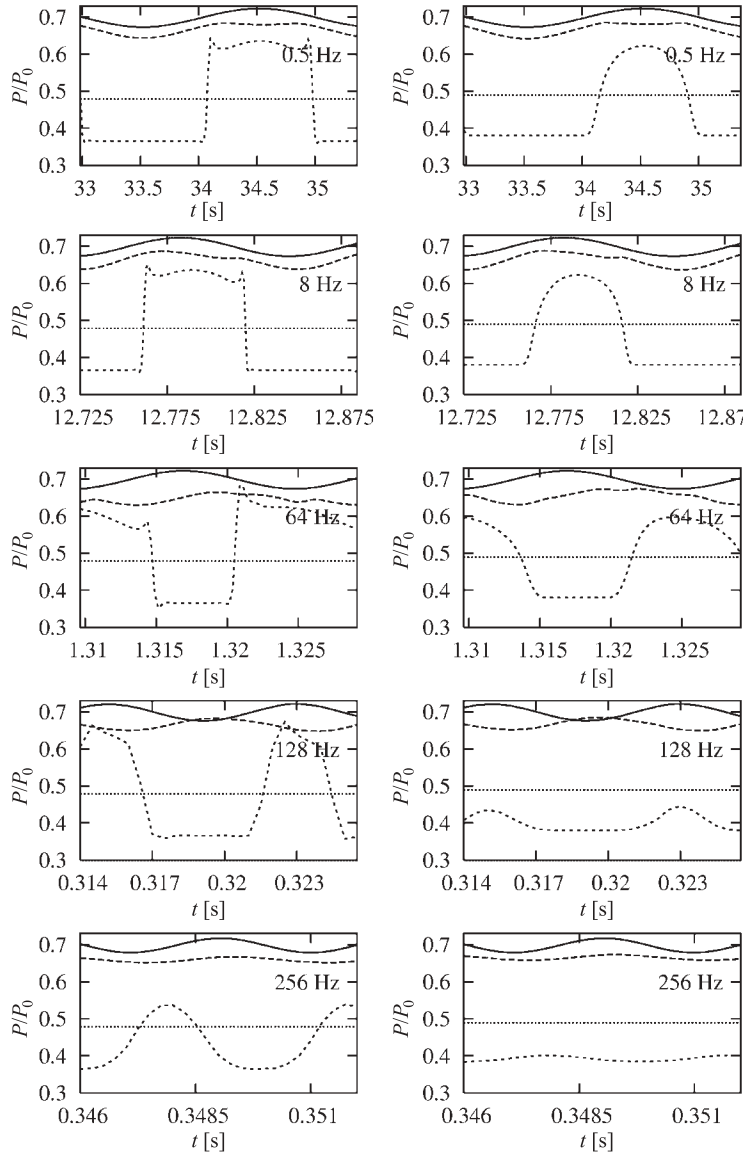

Figure 17. Pressure signals in the middle (left) and at the wall (right) of the nozzle: ····· $x = 0.0$; - - - - $x = 0.15$ (left) and $x = 0.13$ (right); - - - $x = 0.3$; —— $x = 0.9$

A comparison of the oscillation phase at the outlet of the nozzle and at any distant point reveals the lag due to the finite speed of disturbance propagation. It is especially evident for higher frequencies, when the characteristic time of oscillation is short compared with the time taken by the pressure disturbance to reach the shock. Globally, the amplitude of the pressure signal decreases with increasing frequency. Moreover, it can be observed that the signal at the wall decreases to much greater extent than in the middle of the channel. This is due to the shock-boundary layer interaction and the movement of the local acceleration region just downstream of the shock.

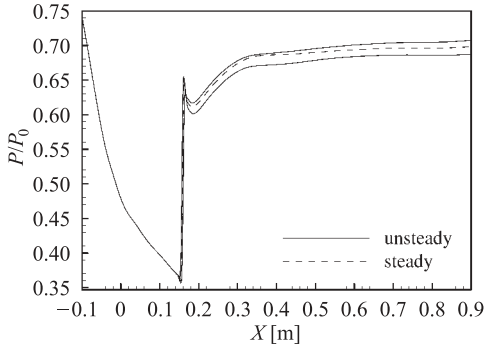

Figure 18. Pressure in the middle of the nozzle, steady state and the unsteady case with 8Hz

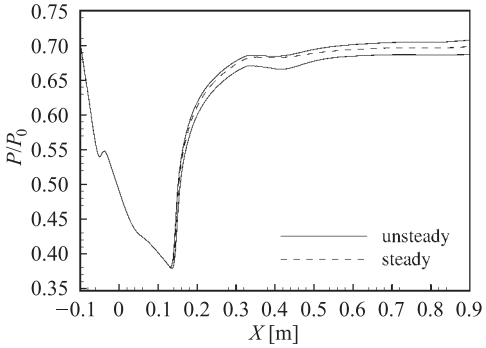

Figure 19. Pressure at the wall of the nozzle, steady state and the unsteady case with 8Hz

In Figures 18 and 19 pressure distributions are presented for the steady case (dashed line) and the 8Hz unsteady case (solid line), where the shock wave is at exactly the same position while moving upstream or downstream the channel. Although the shock wave is at the same location in the nozzle for all cases, the steady state computation differs from the unsteady one. Unsteady pressure downstream of the shock bears little resemblance to the steady state distribution. The potential appearance of shock wave oscillations on an aircraft's wing may introduce large unsteady loads very different from the predicted steady-state values.

7. The flow at high frequencies of excitation

When pressure variation at the outlet is of a high frequency, the shock wave ceases to respond to forced excitations. In such cases it has been observed that a new natural oscillation of the shock appears. This oscillation is of considerably lower frequency and insensitive to forced oscillation. The observed shock oscillation is connected with the formation and shedding of vortices from the separation zone downstream of the shock wave. The effect is illustrated in Figures 20 and 21, which show pressure changes in time at four locations at the wall with and without forced excitation, respectively. The time interval shown in both plots is the same.

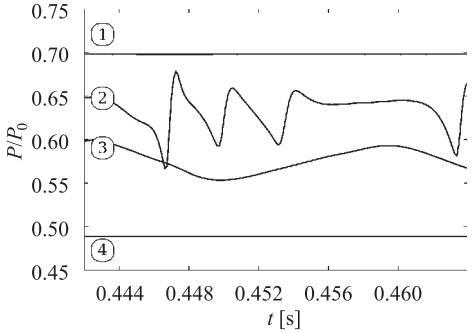

Figure 20. Pressure signals at the nozzle's wall without forced oscillation

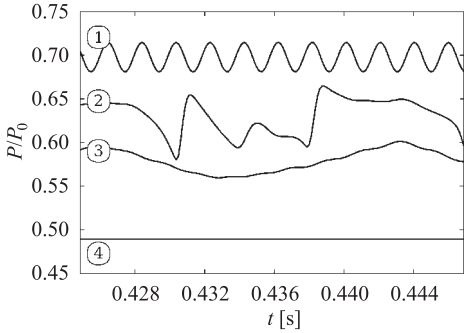

Figure 21. Pressure signals at the nozzle's wall for the 512Hz case

The topmost curve (1) in both diagrams shows the exit pressure (the highest value). It is periodic in Figure 21 and constant in Figure 20. The immediately lower curve (2) shows the pressure change at the location where vortices are formed and shed. The character of these two curves is very similar in both of the figures. Without excitation (Figure 20) the vortices are stronger and exhibit more pronounced pressure extrema. It may be concluded that pressure excitation at the outlet diminishes the strength of the shed vortices. The next lower curve (3) shows the pressure under the front branch of the λ-foot. In fact, it indicates the movement of the shock wave. Outlet pressure excitation makes the distribution line in Figure 21 faintly wavy. The line in Figure 20 has the same amplitude and frequency as the corresponding line in Figure 21 but it is smooth, as there is no excitation. The bottom curve (4) shows the pressure upstream of the shock wave and does not exhibit any effect of the investigated process because it is located in the supersonic part of the flow.

Disappearance of the pressure fluctuations' effect on shock oscillations does not mean that a quasi-steady flow may be obtained. Natural oscillation of the shock wave remains independently from the excitation.

Along the lower wall downstream the shock, the streamlines deviate from the wall making room for a separation (Figure 22). There are local pressure minima at some distance from the shock, which exhibit significant variations in time. These pressure minima indicate the formation of vortices in the separated flow area and prove that this is an unsteady process.

8. Conclusions

The present investigation has provided an insight into the nature of transonic flow in a two-dimensional Laval nozzle for steady and unsteady flow conditions. The general features of such flows were studied by means of the SPARC computer code, which solves the time-dependent, Reynolds-averaged, compressible Navier-Stokes equations with a linear and an adaptive, non-linear, k-τ turbulence closure.

The comparison of numerical predictions and the experiment was satisfactory in the case of steady flows as the Mach numbers were low (1.2–1.4). However, the unavoidable presence of three-dimensionality in the experimental flow decreased the applicability of two-dimensional simulations.

In the unsteady flow cases, the variation of the shock's position and structure as well as the behavior of the flow upstream and downstream of the shock were analyzed numerically for various excitation frequencies ranging from 0Hz to 1024Hz. Computations of the flow predicted most of the essential features observed experimentally by other researchers for similar geometrical configurations and flow conditions.

All the observations revealed differences in the shock wave behavior between the bottom wall and the middle of the channel. The amplitude of the shock wave movement decreased with increasing excitation frequency for both locations. A closer study of low frequencies ($f < 50$Hz) revealed the maximum amplitude of the shock wave movement. For moderate frequencies, the amplitude of the shock motion was inversely proportional to the forcing oscillations.

At 500Hz, the forced shock wave displacement disappeared. Natural oscillations were observed for higher excitations.

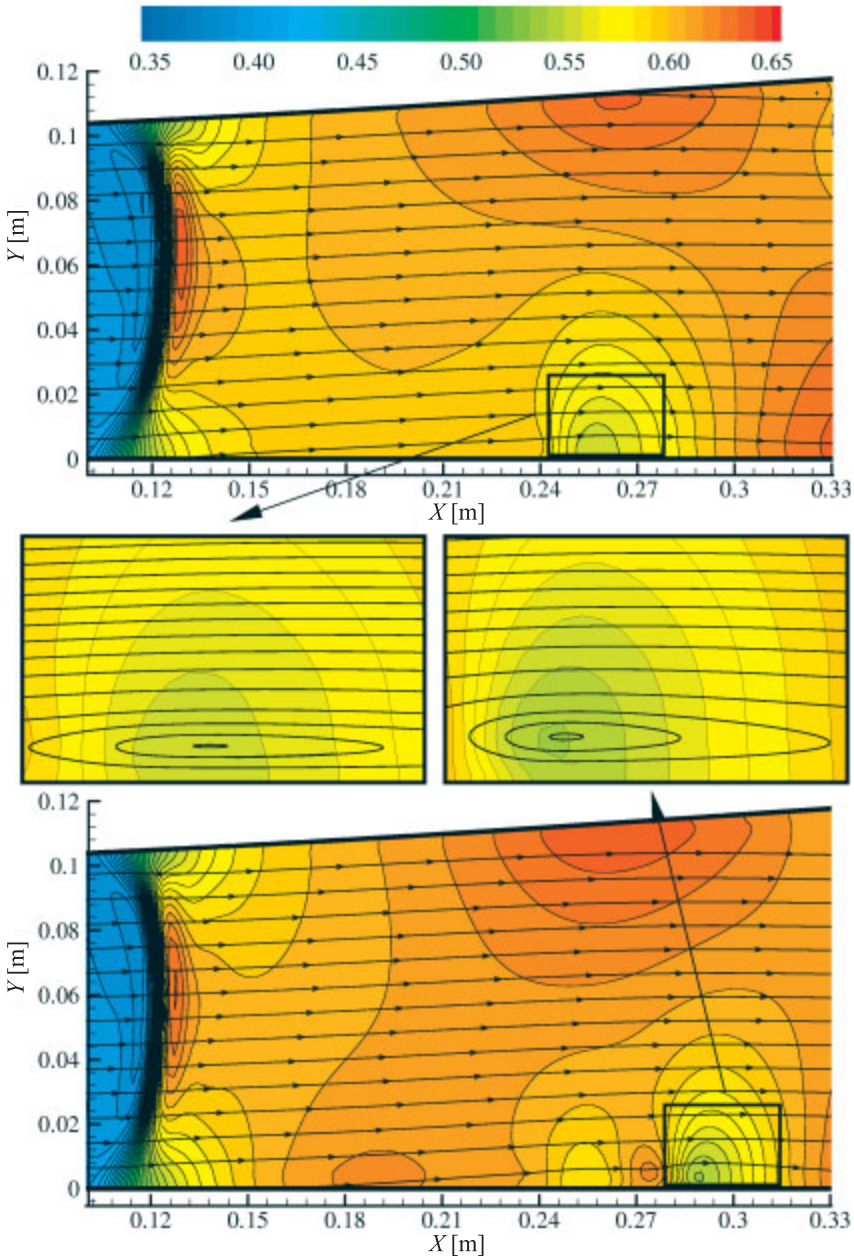

Figure 22. Static pressure maps and streamlines: natural vortex shedding in the separation zone

The unsteady flow appeared to be very different from the steady-state flow field. The pressure jump and the unsteady pressure downstream of the shock were different for identical shock positions during one cycle of fluctuations.

Further experimental and numerical investigations are necessary to validate the local amplitude maximum in the low frequency range. Taking into account the three-dimensional effects of the real flow may significantly improve coincidence of the results.

References

[1] Szulc O 2001 *Unsteady Transonic Flow in the Laval Nozzle*, MSc Thesis, Faculty of Technical Physics and Applied Mathematics, Technical University of Gdansk, Poland (in Polish)
[2] Magagnato F 1998 *TASK Quart.* **2** (2) 215
[3] Magagnato F 2000 *Proc. 8th Int. Symp. on Transport Phenomena and Dynamics of Rotating Machinery*, Honolulu, Hawaii, C557/139/99
[4] Magagnato F 2001 *Proc. CFD for Turbomachinery Applications*, Gdansk, Poland, CFDTurbo-2001-K05
[5] Craft T J, Launder B E and Suga K 1993 *Proc. 5th IAHR Conf. on Refined-Flow Modeling and Turbulence Measurement*, Paris, France
[6] Adamson T C 1972 *J. Fluid Mech.* **52** (3) 437
[7] Adamson T C and Richey G K 1973 *J. Fluid Mech.* **60** (2) 363
[8] Richey G K and Adamson T C 1976 *AIAA Journal* **14** (8) 1054
[9] Chan J S-K and Adamson T C 1978 *AIAA Journal* **16** (4) 377
[10] Adamson T C Jr, Messiter A F and Liou M S 1978 *AIAA Journal* **16** (12) 1240
[11] Messiter A F and Adamson T C Jr 1984 *AIAA Journal* **22** (11) 1590
[12] Rizetta D P and Chin W C 1979 *AIAA Journal* **17** (7) 779
[13] Bölcs A, Fransson T H and Platzer M F 1989 *J. Turbomachinery* **111** (July) 169
[14] Ott P 1992 *Oszillierender senkrechter verdichtungsstoss in einer ebenen düse*, Lausanne EPFL
[15] Ott P, Bölcs A and Fransson T H 1995 *J. Turbomachinery* **117** (January) 106
[16] Seegmiller H L, Marvin J G and Levy L L Jr 1978 *AIAA Journal* **16** (12) 1262
[17] Chen C P, Sajben M and Kroutil J C 1979 *AIAA Journal* **17** (10) 1076
[18] Liou M S and Coakley T J 1984 *AIAA Journal* **22** (8) 1139
[19] Arnone A, Liou M S and Povinelli L A 1995 *AIAA Journal* **33** (6) 985
[20] Gerolymos G A, Vallet I, Bölcs A and Ott P 1996 *AIAA Journal* **34** (7) 1331
[21] Bron O, Ferrand P and Fransson T 2002 *Proc. 9th Int. Symp. on Transport Phenomena and Dynamics of Rotating Machinery*, Honolulu, Hawaii, pp. 1–9
[22] Setoguchi T, Matsuo S and Kim H D 2003 *Proc. Symp. on Shock Waves*, Japan, pp. 49–52
[23] Rieger H and Jameson A 1987 *AIAA paper* **87-0619** 1
[24] Tatsumi S, Martinelli L and Jameson A 1995 *AIAA Journal* **33** (2) 252
[25] Swanson R C, Radespiel R and Turkel E 1997 *NASA, CR-201726 ICASE Report* No. 97-40
[26] Carpenter M H, Gottlieb D, Abarbanel S and Don W S 1993 *NASA, CR-191561 ICASE Report* No. 93-83